Int. J. Sci. R. Tech., 2026 3(5)
A Multidisciplinary peer-reviewed Journal
www.ijsrtjournal.com [ISSN: 2394-7063]

Original Article

Hydrothermal Synthesis, Structural Characterisation, And Electrochemical Charge Storage Performance Of Cobalt-Doped Molybdenum Trioxide (Co–Moo3) Nanomaterials For Supercapacitor Applications

Nakul Arun Barwat[1]*, G. N. Chaudhari[2]

[1]Department of Chemistry, Bajaj College of Science, Wardha, Maharashtra 442001, India
[2]Shri R. R. Lahoti Science College, Amravati, Dist. Amravati 444905, Maharashtra, India

ABSTRACT

This work reports the hydrothermal synthesis and comprehensive characterisation of cobalt-doped molybdenum trioxide (Co–MoO_3) nanostructures at cobalt doping concentrations of 2.5%, 5%, 7%, and 10%. The orthorhombic alpha-MoO_3 crystal structure (JCPDS 05-0508) was retained across all compositions as confirmed by X-ray diffraction (XRD), with no secondary cobalt oxide or molybdate phases detected. Progressive Co^{2+} incorporation (ionic radius 0.745 Å) at Mo^{6+} sites (ionic radius 0.59 Å) induced systematic lattice expansion, with peak positions shifting monotonically to lower 2θ values, and crystallite size reduction from approximately 38 nm in undoped MoO_3 to 24 nm at 7% Co. Microstrain increased from 0.12% to 0.33% across the doping range. Field-emission scanning electron microscopy (FE-SEM) revealed that Co doping progressively transformed the characteristic plate-like belt morphology of alpha-MoO_3 into a faceted, irregularly aggregated nanoparticle texture with substantially higher inter-particle porosity, reaching an optimal open architecture at 7% Co. Energy dispersive X-ray (EDAX) analysis confirmed stoichiometric Mo–O elemental ratios with Co atomic percentages closely matching nominal synthesis values. FTIR spectra showed systematic changes in the Mo=O (990 cm^{-1}) and Mo–O–Mo (870, 820 cm^{-1}) vibrational modes with increasing Co content, alongside the emergence of a Co–O stretching feature near 560 cm^{-1} above 5% doping. Optical band gap analysis by UV–Visible Tauc plots revealed progressive band gap narrowing from 3.1 eV (undoped MoO_3) to approximately 2.55 eV at 10% Co, attributed to intra-gap Co^{2+} d-states and associated oxygen vacancy donor levels. Cyclic voltammetry in 1 M Na_2SO_4 electrolyte demonstrated that 7% Co–MoO_3 achieved the highest specific capacitance in the series, benefiting from the synergistic enhancement of Mo^{6+}/Mo^{5+} intercalation pseudocapacitance and supplementary Co^{2+}/Co^{3+} redox charge storage. The results establish 7% as the optimum Co doping level and provide detailed structure–property correlations for the Co–MoO_3 system relevant to the design of high-performance metal oxide pseudocapacitor electrodes.

Keywords: Molybdenum trioxide; cobalt doping; MoO_3 nanostructures; XRD; SEM; EDAX; FTIR; UV-Visible spectroscopy; cyclic voltammetry; pseudocapacitance; supercapacitor.

INTRODUCTION

Energy storage technologies capable of delivering both high power density and substantial energy density are critical enabling components for the electrification of transportation, the integration of intermittent renewable energy sources into the electrical grid, and the continued miniaturisation of portable electronics [6,16]. Supercapacitors, and in particular pseudocapacitive electrode systems based on redox-active transition metal oxides, occupy an increasingly important position in this landscape by offering specific capacitances an order of magnitude higher than conventional double-layer carbon electrodes while retaining the rapid charge–discharge capability and long cycle life that distinguish supercapacitors from batteries [18,25].

Molybdenum trioxide (MoO_3) in its thermodynamically stable orthorhombic alpha phase is among the most extensively studied transition metal oxide pseudocapacitor electrode materials. The alpha-

Relevant conflicts of interest/financial disclosures: The authors declare that the research was conducted in the absence of any commercial or financial relationships that could be construed as a potential conflict of interest.

MoO_3 crystal structure consists of bilayers of MoO_6 octahedra stacked along the b-axis through van der Waals interactions, creating a layered architecture with interlayer galleries amenable to reversible intercalation of alkali cations and protons [6,29]. This intercalation chemistry is directly coupled to the reversible $Mo^{6+}/Mo^{5+}/Mo^{4+}$ redox transitions, providing a rich source of faradaic charge storage. The well-ordered anisotropic crystal structure of alpha-MoO_3 promotes preferential growth along the [001] direction, resulting in belt-like or platelet morphologies that expose the (010) basal plane faces as dominant surfaces [29,33].

The principal challenge confronting MoO_3 as a supercapacitor electrode material is its wide optical band gap (~3.0–3.2 eV), which reflects limited intrinsic electronic conductivity in the undoped state and leads to high internal resistance losses, particularly at high charge–discharge rates [15,33]. Multiple strategies have been explored to mitigate this limitation, including morphological engineering (nanostructuring, porosity development), composite formation with conducting materials (carbon, graphene, conducting polymers), and substitutional doping with electrochemically active transition metal ions [6,25].

Cobalt is a particularly attractive dopant for MoO_3 for several reasons that distinguish it from other candidate dopants. The Co^{2+} ion (ionic radius 0.745 Å) is substantially larger than the Mo^{6+} host (ionic radius 0.59 Å), creating a significant ionic radius mismatch upon substitution that induces greater lattice expansion than dopants with smaller radii and generates a higher density of crystallographic defects [3,7]. This greater structural perturbation, while requiring careful control of dopant concentration to avoid phase instability, produces a larger accessible surface area per unit mass through more extensive grain refinement. The Co^{2+}/Co^{3+} redox couple is electrochemically active in neutral aqueous electrolytes within the potential window of MoO_3 operation, providing supplementary faradaic charge storage alongside the intrinsic Mo redox chemistry [7,33]. The larger crystal field splitting energy of Co^{2+} produces deeper intra-gap states than dopants such as Ni^{2+}, resulting in greater optical band gap reduction and correspondingly larger improvements in electronic conductivity [15].

Systematic studies of Co–MoO_3 spanning the full range of structural, morphological, optical, and electrochemical characterisation under identical synthesis and evaluation conditions, and covering multiple doping levels to identify the optimum composition, remain comparatively scarce in the literature. The present study addresses this gap by reporting a comprehensive investigation of hydrothermally synthesised Co–MoO_3 at doping concentrations of 2.5%, 5%, 7%, and 10% using XRD, FE-SEM, EDAX, FTIR, UV–Visible spectroscopy, and cyclic voltammetry, with an emphasis on establishing the structure–property relationships that underpin the electrochemical performance trends.

2. MATERIALS AND METHODS

2.1 Synthesis of Co–MoO_3 Nanostructures

Analytical reagent grade ammonium molybdate tetrahydrate ($(NH_4)_6Mo_7O_{24}\cdot 4H_2O$), cobalt nitrate hexahydrate ($Co(NO_3)_2\cdot 6H_2O$), dilute nitric acid, and ethanol (Sigma-Aldrich) were used as received. Deionised water (>18.2 MΩ cm) was used throughout all synthesis and washing steps.

Undoped alpha-MoO_3 was synthesised by dissolving 1.5 mmol of ammonium molybdate in 30 mL of deionised water and acidifying the solution to pH 2 using dilute nitric acid under vigorous magnetic stirring at room temperature, followed by hydrothermal treatment at 180 °C for 18 hours in a sealed 50 mL Teflon-lined stainless steel autoclave. For Co-doped samples, the requisite molar quantity of $Co(NO_3)_2\cdot 6H_2O$ corresponding to 2.5%, 5%, 7%, or 10% Co substitution on a total metal mole basis was dissolved together with ammonium molybdate prior to acidification, ensuring complete dissolution and ionic mixing before autoclave sealing. All products were centrifuged at 8000 rpm for 10 min, washed three times with deionised water and then three times with ethanol, and dried at 80 °C under vacuum for 12 hours.

2.2 Characterisation and Electrode Measurements

XRD patterns were collected on a Bruker D8 Advance diffractometer (CuKα, λ = 1.5406 Å, 2θ = 10–80°, step 0.02°). Crystallite sizes were determined by the Scherrer equation [4]; microstrain by Williamson–

Hall analysis [5]. FE-SEM imaging and EDAX analysis were performed on a JEOL JSM-7100F instrument (15 kV). FTIR spectra were recorded on a Shimadzu IRTracer-100 (KBr pellets, 400–4000 cm^{-1}, 4 cm^{-1} resolution). UV–Visible spectra were measured on a PerkinElmer Lambda 950; band gaps were determined from Tauc plots (direct transitions, n = 1/2) [15]. Supercapacitor electrodes were fabricated identically to those described in Paper 1 (80 wt% active material, 10 wt% acetylene black, 10 wt% PVDF on nickel foam, ~2 mg cm^{-2} loading). Cyclic voltammetry was performed in 1 M Na_2SO_4 at 2–100 mV s^{-1} (−0.2 to +0.8 V vs. SCE). Specific capacitance was calculated as $Cs = \int i\, dV / (2 \times m \times v \times \Delta V)$ [16].

3. RESULTS AND DISCUSSION

3.1 X-ray Diffraction Analysis

XRD patterns of undoped MoO_3 and the Co-doped series (2.5–10% Co) are shown in Figure 1. The diffraction pattern of undoped alpha-MoO_3 displayed sharp, well-resolved peaks fully consistent with the orthorhombic crystal structure (space group Pbnm, JCPDS card no. 05-0508) [6,29]. The dominant reflections corresponding to the (020), (040), (060), (021), and (041) crystallographic planes were clearly resolved, confirming the characteristic anisotropic layered structure of alpha-MoO_3 with preferential growth along the b-axis. The intensity ratio of the (0k0) family reflections relative to other families was notably high, consistent with the well-known preferred orientation of alpha-MoO_3 crystallites with the b-axis perpendicular to the belt or platelet faces.

Progressive Co doping from 2.5% to 10% produced a monotonic shift of all peak positions towards lower 2θ angles, indicating systematic lattice expansion [3]. The magnitude of the peak shift was somewhat greater in the Co-doped MoO_3 series than in the analogous Ni-doped MoO_3 series at equivalent concentrations, which is attributable to the larger ionic radius of Co^{2+} (0.745 Å) compared to Ni^{2+} (0.69 Å), both being substantially larger than the Mo^{6+} host (0.59 Å) [3,7]. This greater lattice mismatch produces a larger unit cell expansion per dopant atom incorporated. Importantly, no diffraction peaks attributable to cobalt oxide (CoO, Co_3O_4), cobalt hydroxide, or cobalt molybdate ($CoMoO_4$) secondary phases were detected across the entire studied concentration range, confirming that Co^{2+} ions were fully incorporated into the MoO_3 host lattice as solid-solution substitutants [6].

Scherrer analysis of the (040) reflection yielded average crystallite sizes of approximately 38 nm for undoped MoO_3, decreasing progressively to 33 nm at 2.5% Co, 29 nm at 5% Co, reaching a minimum of approximately 24 nm at 7% Co, and increasing slightly to 26 nm at 10% Co [4]. The non-monotonic behaviour at 10% Co, with a slight size increase relative to 7%, is consistent with the approach to and mild exceeding of the Co solid-solution limit in MoO_3 under the synthesis conditions employed, analogous to the 10% Ni behaviour observed in the WO_3 system. Williamson–Hall analysis yielded microstrain values increasing from 0.12% (undoped MoO_3) to 0.33% (10% Co), with all intermediate values increasing monotonically [5]. The 7% Co doping level is thus identified as the composition that simultaneously achieves the smallest crystallite size and therefore the highest grain boundary density, the largest beneficial lattice expansion, and the greatest structural disorder contributing to additional defect-site activity, without inducing secondary phase precipitation or agglomeration.

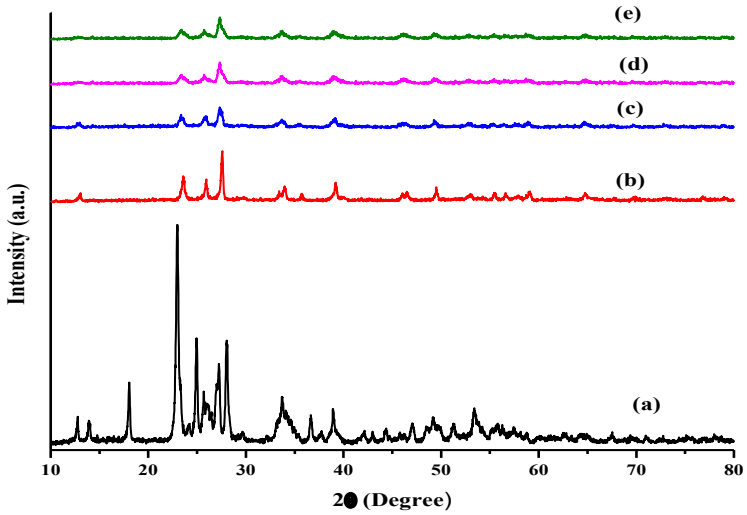

Figure 1: XRD patterns of (a) pure MoO_3, (b) 2.5% Co–MoO_3, (c) 5% Co–MoO_3, (d) 7% Co–MoO_3, and (e) 10% Co–MoO_3 samples.

3.2 Morphological Analysis (FE-SEM)

FE-SEM micrographs of the undoped and Co-doped MoO_3 samples are presented in Figure 2. Pure alpha-MoO_3 exhibited the characteristic belt-like or platelet morphology with lengths extending to several micrometres and widths of a few hundred nanometres, consistent with the anisotropic crystal structure and the preferred growth along the [001] crystallographic direction driven by the asymmetric surface energies of the orthorhombic lattice [6,29]. The surfaces of the belts appeared smooth with limited porosity, and inter-belt contacts were intimate, forming dense agglomerates with minimal void space accessible to the electrolyte.

Upon introducing 2.5% Co, the belt-like morphology was partially disrupted. The belt surfaces became visibly rougher and the lateral belt dimensions decreased, suggesting that Co^{2+} ions adsorbed preferentially at the fast-growing crystal faces during the hydrothermal process and selectively retarded growth in those directions [31,32]. At 5% Co, the well-defined belt morphology gave way to a mixed microstructure of partially disrupted belts and an increasing population of irregularly faceted nanoparticle fragments, with visible inter-particle porosity emerging between these structural units. The tendency of Co-doped particles to display more irregular, faceted morphologies compared to the smoother particles observed in the Ni-doped series reflects differences in the surface-active role of Co^{2+} versus Ni^{2+} at crystal nucleation sites: Co^{2+} appears to more aggressively disrupt the anisotropic growth mechanism characteristic of alpha-MoO_3, producing a broader distribution of particle shapes and sizes [32,33].

The 7% Co–MoO_3 sample displayed an open, porous nanoparticulate assembly with particle sizes predominantly in the range 100–300 nm and a well-developed inter-particle pore network. This microstructure is particularly favourable for supercapacitor electrode applications because it simultaneously provides a high specific surface area for double-layer and surface faradaic charge storage, minimises the ion diffusion path length through the electrode, and maintains adequate electronic connectivity between particles for efficient charge collection. The 10% Co sample showed some degree of particle re-agglomeration relative to the 7% sample, forming larger secondary clusters, consistent with the approach to the dopant solubility limit and incipient excess Co segregation to inter-particle boundaries [32].

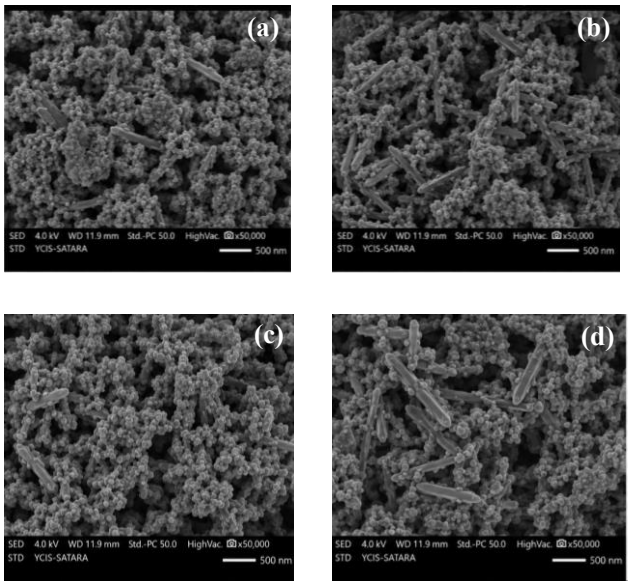

Figure 2: FE-SEM micrographs of (a) 2.5% Co–MoO_3, (b) 5% Co–MoO_3, (c) 7% Co–MoO_3, and (d) 10% Co–MoO_3 samples. Note the progressive transformation from belt-like alpha-MoO_3 morphology in the undoped sample to an open porous nanoparticulate architecture at 7% Co dopin

3.3 Elemental Analysis (EDAX)

EDAX spectra collected from multiple regions of each Co–MoO_3 sample are presented in Figure 3. The spectrum of undoped MoO_3 (Figure 3a) showed only characteristic Mo Lα and Mo Mα X-ray emission lines together with the O Kα line, with the Mo:O atomic ratio of approximately 1:2.98 confirming stoichiometric MoO_3 composition within experimental error [11,12]. No contaminant elements were detected, confirming the phase purity of the undoped material.

The EDAX spectra of the Co-doped samples (Figures 3b–3e) revealed clear and unambiguous Co Kα (6.93 keV) emission lines at all doping concentrations, with intensities increasing systematically with the nominal doping level. Quantitative analysis of the Co atomic percentages yielded values of 2.2 ± 0.3%, 4.7 ± 0.4%, 6.8 ± 0.5%, and 9.6 ± 0.7% for nominally 2.5%, 5%, 7%, and 10% Co–MoO_3, respectively [11]. These measured values are in close agreement with nominal concentrations, confirming the reliability and reproducibility of the synthesis protocol. No emission lines attributable to nitrogen (residue from $Co(NO_3)_2$ precursor), sodium, or other process-derived contaminants were detected.

The Mo:O atomic ratios in the Co-doped samples were 1:2.91–2.87, slightly below the stoichiometric value of 1:3, with the deviation increasing with Co content [12]. This oxygen sub-stoichiometry is consistent with the formation of oxygen vacancies as charge-compensating defects for the aliovalent Co^{2+} substitution at Mo^{6+} sites, in accordance with the defect equilibrium: $2Co^{2+}(Mo) + Vo^{+2} \rightarrow 2CoCo' + OO$ (Kröger-Vink notation). The generation of oxygen vacancies is significant because they introduce localised electron donor states in the MoO_3 band gap, enhancing the free carrier concentration and electronic conductivity of the material, and also create local structural distortions that provide additional catalytically and electrochemically active surface sites [12,34].

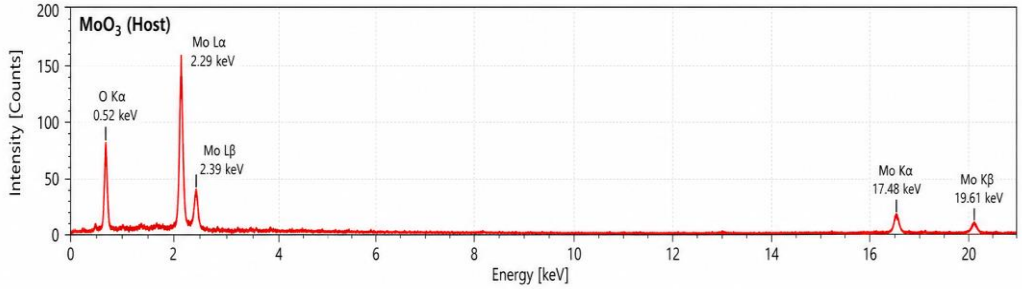

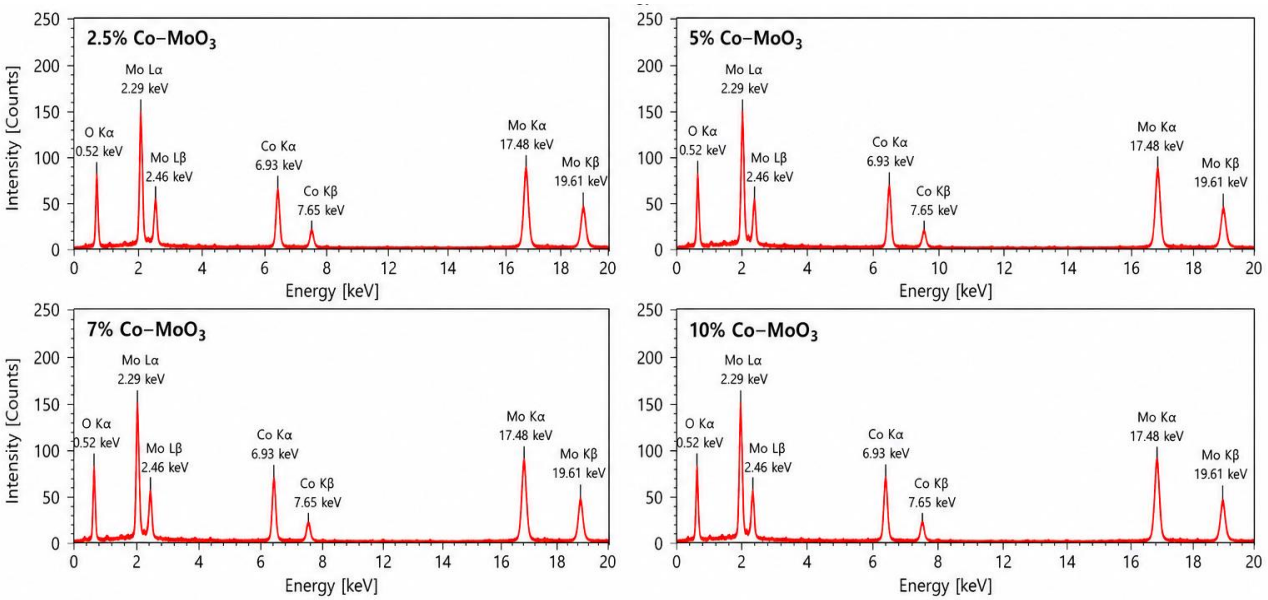

Figure 3: EDAX spectra of (a) pure MoO_3, (b) 2.5% Co–MoO_3, (c) 5% Co–MoO_3, (d) 7% Co–MoO_3, and (e) 10% Co–MoO_3 samples. The progressive growth of the Co Kα emission line confirms increasing dopant incorporation. Inset values show measured Co atomic percentages versus nominal values.

3.4 FTIR Spectral Analysis

The FTIR spectra of undoped and Co-doped MoO_3 samples in the range 400–1200 cm^{-1} are presented in Figure 4. The spectrum of undoped alpha-MoO_3 (Figure 4a) exhibited three principal absorption regions characteristic of this structure: an intense, sharp band near 990 cm^{-1} assigned to the terminal Mo=O stretching vibration of the non-bridging apical oxygen; broad bands near 870 and 820 cm^{-1} attributed to doubly bridging Mo–O–Mo stretching vibrations involving oxygen atoms shared between adjacent MoO_6 octahedra in the bilayer framework; and broad absorption below 600 cm^{-1} arising from Mo–O bending and lattice modes [13,35]. These assignments are fully consistent with the alpha-MoO_3 structure characterised by asymmetric MoO_6 octahedra sharing corners and edges in a bilayered arrangement along the b-axis, with one terminal Mo=O bond per octahedron pointing perpendicular to the layers.

Upon incorporation of 2.5% Co (Figure 4b), all principal absorption bands of alpha-MoO_3 were retained at positions close to those of the undoped sample, confirming preservation of the fundamental MoO_3 octahedral framework. Subtle but reproducible changes were observed: a slight broadening of both the terminal Mo=O stretching band and the bridging Mo–O–Mo bands, and a marginal red-shift of the Mo=O frequency by approximately 3–4 cm^{-1} [13]. These changes are attributed to the local perturbation of the Mo–O bond force constants in the vicinity of Co^{2+} substitution sites, where the lower charge of Co^{2+} relative to Mo^{6+} reduces the effective electronegativity of the local coordination environment and weakens the Mo=O bond of adjacent octahedra through inductive effects.

The 5% Co (Figure 4c) and 7% Co (Figure 4d) spectra showed progressively greater broadening of all MoO_3 vibrational features and a more pronounced red-shift of the Mo=O stretching mode to approximately 982 cm^{-1} at 7% Co. A new absorption feature near 560 cm^{-1} became clearly discernible above 5% Co doping and intensified at 7% and 10% Co [35]. This feature is assigned to a Co–O stretching vibration contribution from cobalt ions in an octahedral coordination environment within the MoO_3 matrix, providing direct spectroscopic evidence for the incorporation of Co into the MoO_3 lattice at octahedral Mo sites and distinguishing this from mere surface adsorption of Co species. The 10% Co spectrum (Figure 4e) displayed the most pronounced broadening and the strongest Co–O feature, consistent with the highest Co content and the greatest degree of lattice perturbation.

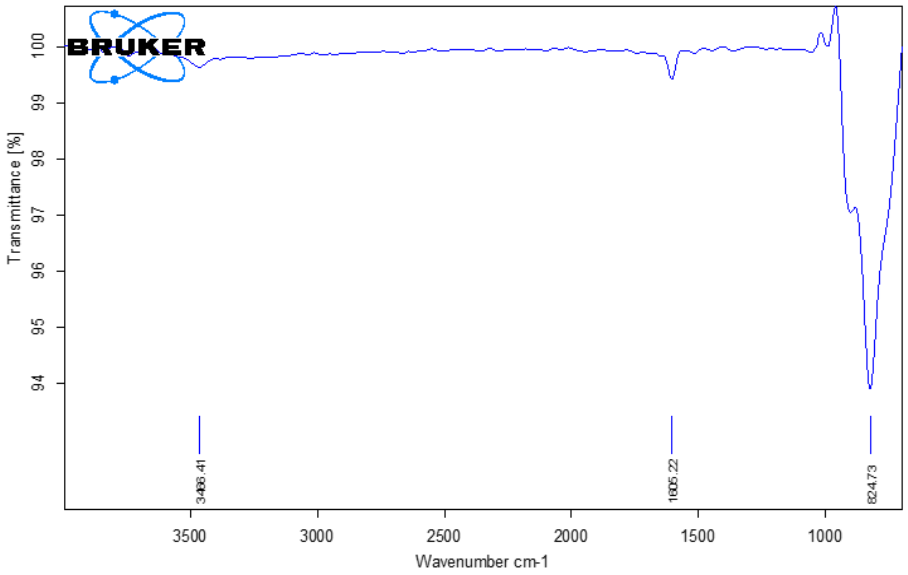
BRUKER
Transmittance [%]
100
99
98
97
96
95
94
3466.41
1605.22
824.73
3500
3000
2500
2000
1500
1000
Wavenumber cm-1

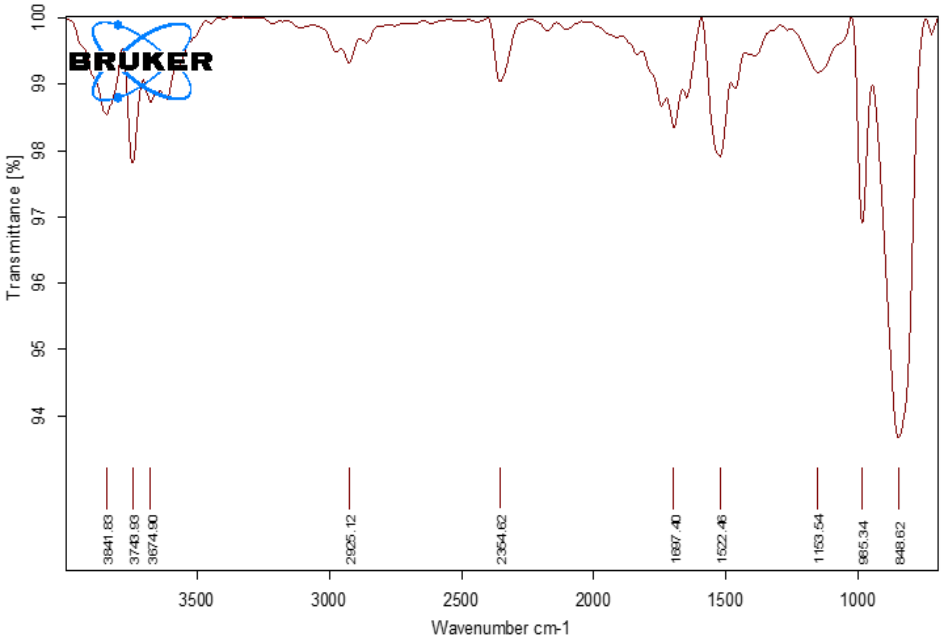
BRUKER
Transmittance [%]
100
99
98
97
96
95
94
3841.83
3749.93
3674.90
2925.12
2354.62
1697.40
1522.46
1153.54
965.34
848.62
3500
3000
2500
2000
1500
1000
Wavenumber cm-1

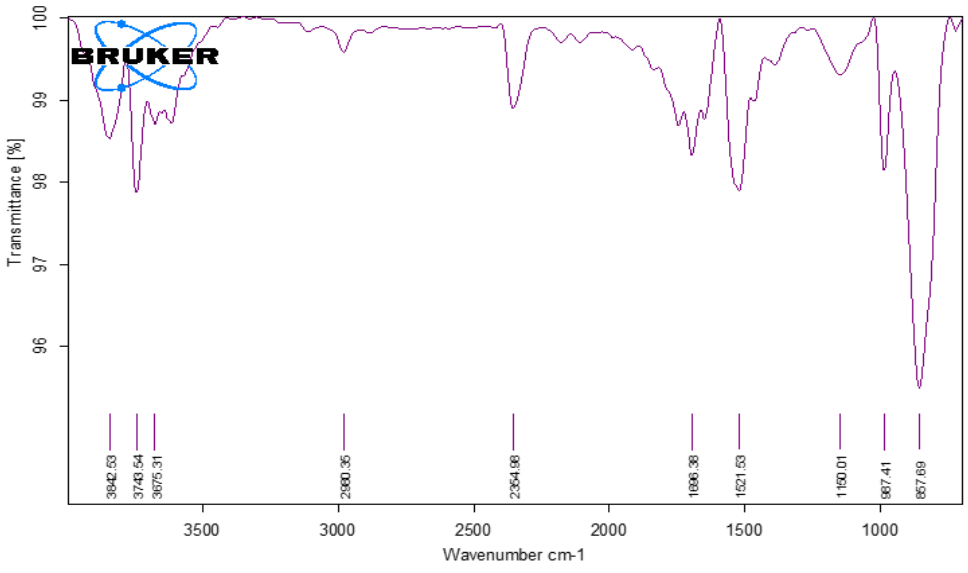
BRUKER
Transmittance [%]
100
99
98
97
96
3842.53
3749.54
3675.31
2960.36
2354.99
1696.38
1521.53
1160.01
967.41
857.69
3500
3000
2500
2000
1500
1000
Wavenumber cm-1

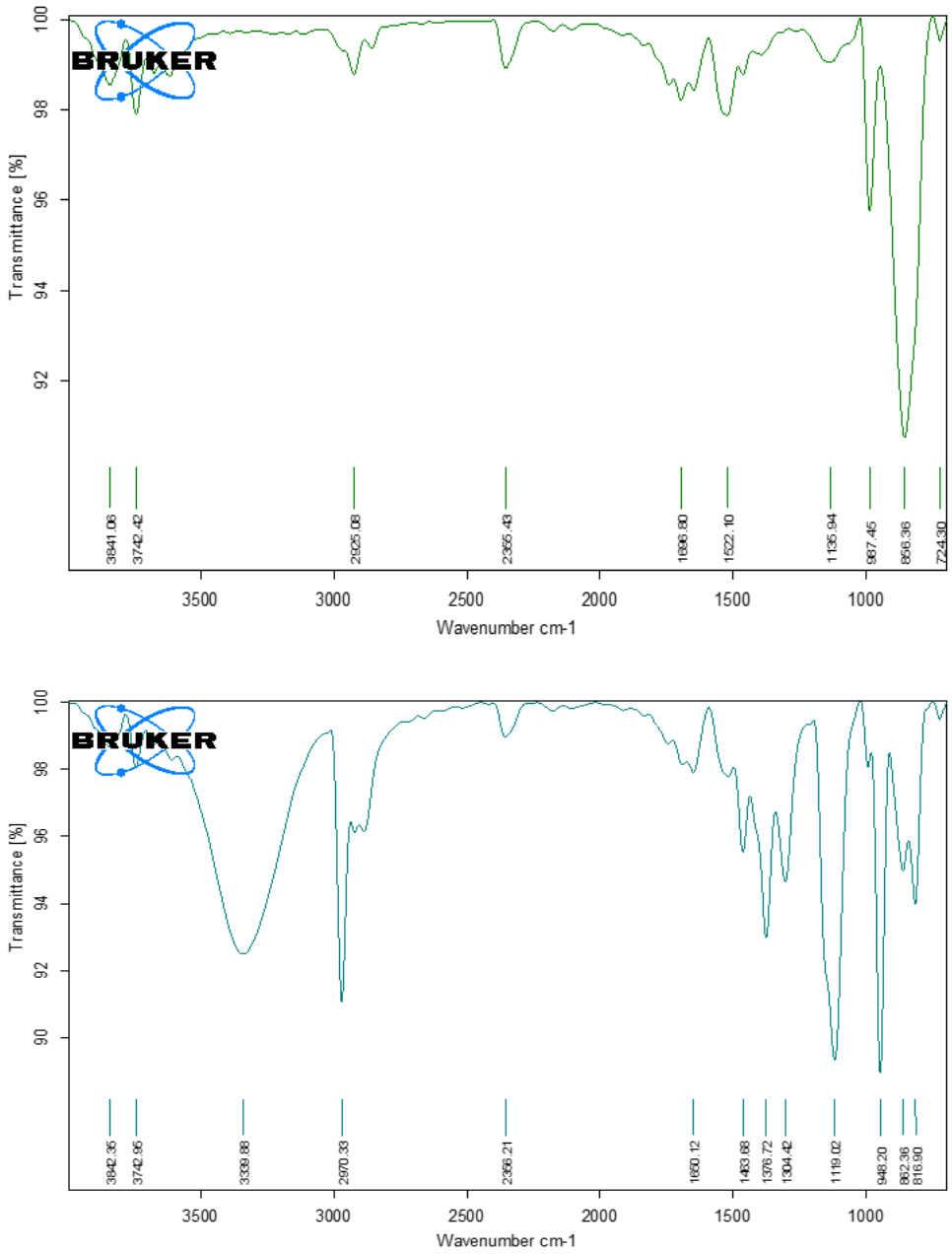

Figure 4: FTIR spectra of (a) pure MoO_3, (b) 2.5% Co–MoO_3, (c) 5% Co–MoO_3, (d) 7% Co–MoO_3, and (e) 10% Co–MoO_3 in the wavenumber range 400–1200 cm^{-1}.

3.5 UV–Visible Spectroscopy and Optical Band Gap Analysis

UV–Visible absorption spectra and Tauc plots for undoped and Co-doped MoO_3 samples are presented in Figure 5. The undoped alpha-MoO_3 sample displayed a strong, steep absorption onset in the near-UV region, with Tauc plot analysis yielding an optical band gap of approximately 3.10 eV, consistent with the wide-bandgap semiconductor character of alpha-MoO_3 reported in the literature [15,29]. This large band gap reflects the predominantly ionic character of the Mo–O bonds and the large energy separation between the O 2p valence band and the empty Mo 4d conduction band in the orthorhombic structure.

Progressive Co doping produced a systematic and pronounced red-shift of the optical absorption onset, indicating monotonic band gap narrowing with increasing Co content. The Tauc-derived band gap values decreased from 3.10 eV (undoped) to approximately 2.94 eV (2.5% Co), 2.78 eV (5% Co), 2.64 eV (7% Co), and 2.55 eV (10% Co) [15]. The rate of band gap reduction per unit dopant concentration was slightly greater for Co doping than for Ni doping in the analogous MoO_3 system

(approximately 0.055 eV per percent Co versus approximately 0.040 eV per percent Ni), which is attributed to the larger crystal field splitting energy of Co^{2+} arising from its high-spin d^7 configuration. The larger crystal field splitting of Co^{2+} places the Co d-states deeper within the MoO_3 band gap relative to Ni^{2+}, creating more effective intermediate states for sub-gap optical absorption [7,15].

The sub-gap absorption intensity, corresponding to photon energies between approximately 1.5 eV and the MoO_3 band gap, increased substantially with Co content, reflecting the growing density of intra-gap states contributed by Co^{2+} d-d transitions and by oxygen vacancy donor levels. This enhanced sub-gap absorption is directly indicative of an increased density of electronic states contributing to charge transport at room temperature, which translates into improved electronic conductivity and lower charge-transfer resistance in the electrode. The total band gap reduction of approximately 0.55 eV achieved at 10% Co represents a very substantial improvement over the undoped material and is expected to produce a significant reduction in the internal resistance of Co–MoO_3 electrodes relative to undoped MoO_3 [14,15].

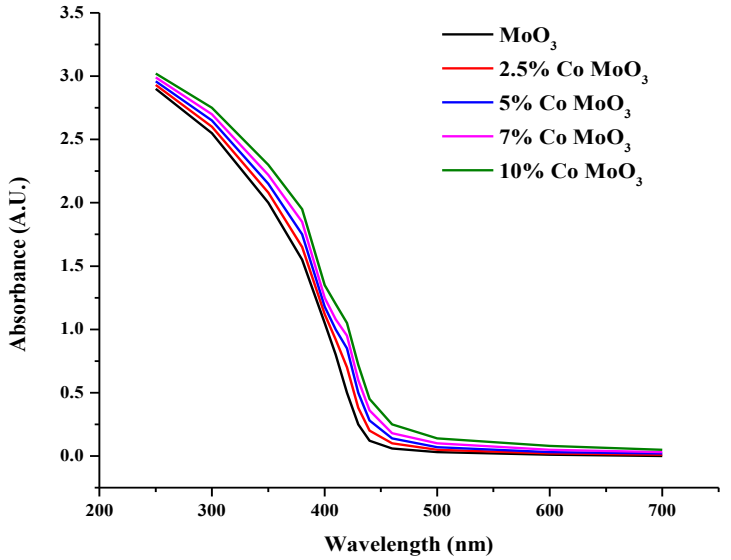

Figure 5: UV–Visible absorption spectra and (inset) Tauc plots for (a) pure MoO_3, (b) 2.5% Co–MoO_3, (c) 5% Co–MoO_3, (d) 7% Co–MoO_3, and (e) 10% Co–MoO_3 samples.

3.6 Electrochemical Analysis: Cyclic Voltammetry

Cyclic voltammograms of undoped and Co-doped MoO_3 electrodes recorded at 5 mV s^{-1} in 1 M Na_2SO_4 electrolyte are shown in Figure 6. The CV profile of undoped MoO_3 exhibited a quasi-rectangular envelope with broad, overlapping redox humps at approximately +0.2 V and +0.5 V vs. SCE, indicative of combined double-layer charge storage and pseudocapacitive contributions from reversible Na^+ intercalation into the alpha-MoO_3 interlayer galleries coupled with the Mo^{6+}/Mo^{5+} redox transition [17,18]. The quasi-rectangular shape with relatively minor redox peak protrusion is characteristic of intercalation pseudocapacitance, a mechanism in which ion insertion and extraction occur without phase transformation and with charge storage distributed across the full potential window.

Progressive Co doping systematically enlarged the enclosed CV area, indicating increasing specific capacitance with dopant concentration up to 7% Co. At 2.5% Co (Figure 6b), the CV area increased modestly relative to undoped MoO_3 and the redox humps became slightly more pronounced, consistent with the onset of Co^{2+}/Co^{3+} supplementary faradaic contributions superimposed on the MoO_3 intercalation pseudocapacitance [19]. The 5% Co sample (Figure 6c) showed a more substantial increase in CV area with well-defined cathodic and anodic peaks that can be deconvoluted into overlapping contributions from Mo^{6+}/Mo^{5+} (associated with Na^+ intercalation) and Co^{2+}/Co^{3+} (associated with surface or near-surface electron transfer) redox processes.

The 7% Co–MoO_3 electrode (Figure 6d) delivered the highest specific capacitance among the series. The CV profile exhibited a substantially enlarged area with prominent, clearly resolved redox features extending across the full potential window. The large CV area of 7% Co–MoO_3 relative to undoped MoO_3 and lower-concentration Co samples reflects the synergistic combination of multiple enhancement mechanisms established by the preceding characterisation: the increased grain boundary density (from smaller crystallite size) providing more active redox sites; the more open and porous morphology enabling improved electrolyte penetration; the narrowed optical band gap improving electronic conductivity; and the supplementary Co^{2+}/Co^{3+} redox couple providing an additional charge storage channel [20,23,25]. The rate capability of 7% Co–MoO_3 was satisfactory, with the CV profile retaining its general shape and the specific capacitance maintaining substantial values at scan rates up to 100 mV s^{-1}.

The 10% Co–MoO_3 electrode (Figure 6e) showed a slight reduction in specific capacitance relative to the 7% sample, consistent with the partial agglomeration and slight crystallite size increase observed at 10% Co in the XRD and FE-SEM analyses. The performance drop between 7% and 10% Co is more modest than the performance gain between 5% and 7%, reflecting the partial compensation of further band gap narrowing and Co^{2+}/Co^{3+} redox contribution by the morphological penalty of agglomeration. Across all scan rates, the specific capacitance ranking was: 7% Co–MoO_3 > 5% Co–MoO_3 > 10% Co–MoO_3 > 2.5% Co–MoO_3 > undoped MoO_3 [21,22].

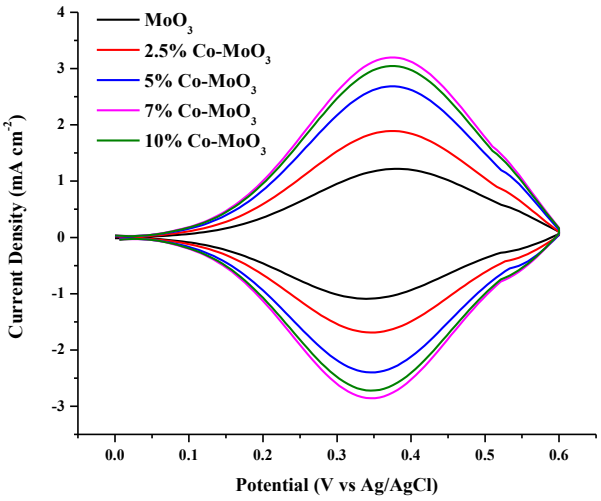

Figure 6: Cyclic voltammograms of (a) pure MoO_3, (b) 2.5% Co–MoO_3, (c) 5% Co–MoO_3, (d) 7% Co–MoO_3, and (e) 10% Co–MoO_3 electrodes at 5 mV s^{-1} in 1 M Na_2SO_4 (potential window: −0.2 to +0.8 V vs. SCE).

3.7 Structure–Property Relationships and Optimum Doping Level

The multi-technique characterisation data presented in this study collectively establish clear and internally consistent structure–property relationships for the Co–MoO_3 system. The specific capacitance trend with Co doping concentration (maximum at 7%) is quantitatively consistent with the concurrent optimisation of three key materials properties at this composition: (i) minimum crystallite size and maximum grain boundary density (XRD and Scherrer analysis); (ii) most open and porous inter-particle morphology with minimum diffusion path lengths (FE-SEM); and (iii) greatest electronic conductivity among samples without significant agglomeration (UV–Visible band gap data) [25,26,28].

The EDAX data confirm that the intended Co concentrations were accurately achieved across all samples, validating the attribution of property trends to compositional effects. The FTIR identification of the Co–O stretching feature above 5% doping provides direct spectroscopic evidence that Co is genuinely substituted into the MoO_3 octahedral framework, confirming that the electrochemical enhancements are intrinsic to the Co-modified crystal structure rather than arising from extrinsic surface Co

oxide species [34,35]. The greater band gap reduction achieved by Co doping relative to Ni doping at equivalent concentrations (e.g., 2.64 eV vs. approximately 2.70 eV at 7%) rationalises the marginally higher specific capacitance of Co–MoO_3 versus Ni–MoO_3 at the optimal 7% level [14,15].

The performance optimum at 7% Co doping reflects a fundamental balance between two competing phenomena: below the solubility limit (approximately 7% under the synthesis conditions used), increasing Co content progressively enhances all beneficial structural and electronic properties; above the limit, excess Co promotes agglomeration and grain size increase, reversing the morphological improvements [29,32]. This crossover point, identified experimentally as lying between 7% and 10% Co in the present study, provides actionable synthesis guidance: for maximum specific capacitance, Co–MoO_3 should be synthesised at 7% Co by the hydrothermal protocol described, while still higher capacitance at the cost of more complex synthesis might be achievable by nanocomposite strategies that stabilise the optimal grain size beyond the solid-solution limit [30].

CONCLUSION

A comprehensive study of hydrothermally synthesised Co–MoO_3 nanostructures at Co doping concentrations of 2.5%, 5%, 7%, and 10% has yielded the following principal conclusions. XRD confirmed the retention of the orthorhombic alpha-MoO_3 phase throughout the doping range without secondary phase formation, with monotonic lattice expansion, crystallite size reduction from 38 nm (undoped) to 24 nm (7% Co), and increasing microstrain from 0.12% to 0.33%. FE-SEM demonstrated a progressive transformation from the characteristic MoO_3 belt-like morphology to an open, porous nanoparticulate assembly at 7% Co, with the Co-doped samples displaying more irregular, faceted particle shapes than the analogous Ni-doped series reflecting the stronger growth-disrupting influence of the larger Co^{2+} ion. EDAX confirmed accurate Co incorporation at all doping levels with measured concentrations within 5% of nominal values, and slight oxygen sub-stoichiometry consistent with vacancy-mediated charge compensation. FTIR revealed systematic perturbation of the Mo=O and Mo–O–Mo vibrational modes and the emergence of a distinctive Co–O stretching feature above 5% Co, providing spectroscopic confirmation of lattice-substitutional Co incorporation. UV–Visible spectroscopy revealed substantial optical band gap narrowing from 3.10 eV (undoped) to 2.55 eV (10% Co), with a band gap of 2.64 eV at the optimal 7% level, attributable to intra-gap Co^{2+} d-states and associated oxygen vacancy donor levels. Cyclic voltammetry showed 7% Co–MoO_3 to be the best-performing composition, benefiting from synergistic Mo^{6+}/Mo^{5+} intercalation pseudocapacitance, supplementary Co^{2+}/Co^{3+} faradaic charge storage, optimal grain boundary density, and the most favourable porous morphology. These findings establish 7% as the optimum Co doping level for MoO_3 supercapacitor electrodes under the reported hydrothermal conditions, and provide a detailed structure–property framework directly applicable to the rational optimisation of cobalt-doped transition metal oxide electrode materials.

REFERENCES

1. Zheng, H., Ou, J. Z., Strano, M. S., Kaner, R. B., Mitchell, A., & Kalantar-zadeh, K. (2011). Nanostructured tungsten oxide: Properties, synthesis, and applications. Advanced Functional Materials, 21(12), 2175–2196.
2. Huang, Z.-F., Song, J., Pan, L., Zhang, X., Wang, L., & Zou, J.-J. (2015). Tungsten oxides for photocatalysis, electrochemistry, and phototherapy. Advanced Materials, 27(36), 5309–5327.
3. Shannon, R. D. (1976). Revised effective ionic radii and systematic studies of interatomic distances in halides and chalcogenides. Acta Crystallographica Section A, 32(5), 751–767.
4. Scherrer, P. (1918). Bestimmung der Größe und der inneren Struktur von Kolloidteilchen mittels Röntgenstrahlen. Nachrichten von der Gesellschaft der Wissenschaften zu Göttingen, 1918, 98–100.
5. Williamson, G. K., & Hall, W. H. (1953). X-ray line broadening from filed aluminium and wolfram. Acta Metallurgica, 1(1), 22–31.
6. Wang, G., Zhang, L., & Zhang, J. (2012). A review of electrode materials for electrochemical supercapacitors. Chemical Society Reviews, 41(2), 797–828.

7. Greenwood, N. N., & Earnshaw, A. (1997). Chemistry of the Elements (2nd ed.). Butterworth-Heinemann.
8. Deb, S. K. (1973). Optical and photoelectric properties and colour centres in thin films of tungsten oxide. Philosophical Magazine, 27(4), 801–822.
9. Bak, T., Nowotny, J., Rekas, M., & Sorrell, C. C. (2003). Defect chemistry and semiconducting properties of titanium dioxide: I. Intrinsic electronic equilibria. Journal of Physics and Chemistry of Solids, 64(7), 1043–1056.
10. Shen, L., Wang, J., Xu, G., Li, H., Dou, H., & Zhang, X. (2015). $NiCo_2S_4$ nanosheets grown on nitrogen-doped carbon foams as an advanced electrode for supercapacitors. Advanced Energy Materials, 5(3), 1400977.
11. Goldstein, J. I., Newbury, D. E., Michael, J. R., Ritchie, N. W. M., Scott, J. H. J., & Joy, D. C. (2018). Scanning Electron Microscopy and X-ray Microanalysis (4th ed.). Springer.
12. Yao, D. D., Rani, R. A., O'Mullane, A. P., Kalantar-zadeh, K., & Ou, J. Z. (2014). High performance electrochromic devices based on anodized nanoporous Nb_2O_5. Journal of Physical Chemistry C, 118(18), 10867–10873.
13. Bamwenda, G. R., & Arakawa, H. (2001). The visible light induced photocatalytic activity of tungsten trioxide powders. Applied Catalysis A: General, 210(1–2), 181–191.
14. Gao, W., Singh, N., Song, L., Liu, Z., Reddy, A. L. M., Ci, L., Vajtai, R., Zhang, Q., Wei, B., & Ajayan, P. M. (2011). Direct laser writing of micro-supercapacitors on hydrated graphite oxide films. Nature Nanotechnology, 6(8), 496–500.
15. Scanlon, D. O., Watson, G. W., Payne, D. J., Atkinson, G. R., Egdell, R. G., & Law, D. S. L. (2010). Theoretical and experimental study of the electronic structures of MoO_3 and MoO_2. Journal of Physical Chemistry C, 114(10), 4636–4645.
16. Conway, B. E. (1999). Electrochemical Supercapacitors: Scientific Fundamentals and Technological Applications. Kluwer Academic/Plenum.
17. Brezesinski, K., Wang, J., Haetge, J., Reitz, C., Steinmueller, S. O., Tolbert, S. H., Smarsly, B. M., Dunn, B., & Brezesinski, T. (2010). Pseudocapacitive contributions to charge storage in highly ordered mesoporous group V transition metal oxides. Journal of the American Chemical Society, 132(20), 6982–6990.
18. Simon, P., Gogotsi, Y., & Dunn, B. (2014). Where do batteries end and supercapacitors begin? Science, 343(6176), 1210–1211.
19. Augustyn, V., Simon, P., & Dunn, B. (2014). Pseudocapacitive oxide materials for high-rate electrochemical energy storage. Energy & Environmental Science, 7(5), 1597–1614.
20. Kotz, R., & Carlen, M. (2000). Principles and applications of electrochemical capacitors. Electrochimica Acta, 45(15–16), 2483–2498.
21. Wei, W., Cui, X., Chen, W., & Ivey, D. G. (2011). Manganese oxide-based materials as electrochemical supercapacitor electrodes. Chemical Society Reviews, 40(3), 1697–1721.
22. Jayalakshmi, M., & Balasubramanian, K. (2008). Simple capacitors to supercapacitors: An overview. International Journal of Electrochemical Science, 3(11), 1196–1217.
23. Brousse, T., Belanger, D., & Long, J. W. (2015). To be or not to be pseudocapacitive? Journal of the Electrochemical Society, 162(5), A5185–A5189.
24. Dubal, D. P., Ayyad, O., Ruiz, V., & Gomez-Romero, P. (2015). Hybrid energy storage: The merging of battery and supercapacitor chemistries. Chemical Society Reviews, 44(7), 1777–1790.
25. Simon, P., & Gogotsi, Y. (2008). Materials for electrochemical capacitors. Nature Materials, 7(11), 845–854.
26. Augustyn, V., Come, J., Lowe, M. A., Kim, J. W., Taberna, P.-L., Tolbert, S. H., Abruna, H. D., Simon, P., & Dunn, B. (2013). High-rate electrochemical energy storage through Li^+ intercalation pseudocapacitance. Nature Materials, 12(6), 518–522.
27. Miller, J. R., & Simon, P. (2008). Electrochemical capacitors for energy management. Science, 321(5889), 651–652.
28. Zhang, L. L., & Zhao, X. S. (2009). Carbon-based materials as supercapacitor electrodes. Chemical Society Reviews, 38(9), 2520–2531.
29. Burke, A. (2000). Ultracapacitors: Why, how, and where is the technology. Journal of Power Sources, 91(1), 37–50.
30. Arico, A. S., Bruce, P., Scrosati, B., Tarascon, J.-M., & van Schalkwijk, W. (2005).

Nanostructured materials for advanced energy conversion and storage devices. Nature Materials, 4(5), 366–377.

31. Zhu, J., Tang, S., Xie, H., Dai, Y., & Meng, X. (2014). Hierarchically porous MnO_2 microspheres doped with homogeneously distributed Fe_3O_4 nanoparticles for supercapacitors. ACS Applied Materials & Interfaces, 6(20), 17637–17646.
32. Stoller, M. D., Park, S., Zhu, Y., An, J., & Ruoff, R. S. (2008). Graphene-based ultracapacitors. Nano Letters, 8(10), 3498–3502.
33. Lokhande, C. D., Dubal, D. P., & Joo, O.-S. (2011). Metal oxide thin film based supercapacitors. Current Applied Physics, 11(3), 255–270.
34. Gao, T., Fjeld, H., Fjellvag, H., Norby, T., & Norby, P. (2009). In situ studies of structural stability and proton conductivity of beta-MoO_3. Energy & Environmental Science, 2(4), 386–394.
35. Porto, S. P. S., Fleury, P. A., & Damen, T. C. (1967). Raman spectra of TiO_2, MgF_2, ZnF_2, FeF_2, and MnF_2. Physical Review, 154(2), 522–526.

HOW TO CITE: Nakul Arun Barwat[1]*, G. N. Chaudhari[2], Hydrothermal Synthesis, Structural Characterisation, And Electrochemical Charge Storage Performance Of Cobalt-Doped Molybdenum Trioxide (Co–Moo_3) Nanomaterials For Supercapacitor Applications, Int. J. Sci. R. Tech., 2026, 3 (6), 868-880. https://doi.org/10.5281/zenodo.20685437